JOURNAL OF GEOPHYSICAL RESEARCH: SPACE PHYSICS, VOL. 118, 7611–7623, doi:10.1002/2013JA019228, 2013

Determining the spectra of radiation belt electron losses: Fitting DEMETER electron flux observations for typical and storm times

Ian C. Whittaker,[1] Rory J. Gamble,[1] Craig J. Rodger,[1] Mark A. Clilverd,[2] and Jean-André Sauvaud[3]

Received 16 July 2013; revised 21 October 2013; accepted 6 November 2013; published 9 December 2013.

[1] The energy spectra of energetic electron precipitation from the radiation belts are studied in order to improve our understanding of the influence of radiation belt processes. The Detection of Electromagnetic Emissions Transmitted from Earthquake Regions (DEMETER) microsatellite electron flux instrument is comparatively unusual in that it has very high energy resolution (128 channels with 17.9 keV widths in normal survey mode), which lends itself to this type of spectral analysis. Here electron spectra from DEMETER have been analyzed from all six years of its operation, and three fit types (power law, exponential, and kappa-type) have been applied to the precipitating flux observations. We show that the power law fit consistently provides the best representation of the flux and that the kappa-type is rarely valid. We also provide estimated uncertainties in the flux for this instrument as a function of energy. Average power law gradients for nontrapped particles have been determined for geomagnetically nondisturbed periods to get a typical global behavior of the spectra in the inner radiation belt, slot region, and outer radiation belt. Power law spectral gradients in the outer belt are typically –2.5 during quiet periods, changing to a softer spectrum of ∼ –3.5 during geomagnetic storms. The inner belt does the opposite, hardening from –4 during quiet times to ∼ –3 during storms. Typical outer belt *e*-folding values are ∼200 keV, dropping to ∼150 keV during geomagnetic storms, while the inner belt *e*-folding values change from ∼120 keV to >200 keV. Analysis of geomagnetic storm periods show that the precipitating flux enhancements evident from such storms take approximately 13 days to return to normal values for the outer belt and slot region and approximately 10 days for the inner belt.

Citation: Whittaker, I. C., R. J. Gamble, C. J. Rodger, M. A. Clilverd, and J.-A. Sauvaud (2013), Determining the spectra of radiation belt electron losses: Fitting DEMETER electron flux observations for typical and storm times, *J. Geophys. Res. Space Physics*, *118*, 7611–7623, doi:10.1002/2013JA019228.

1. Introduction

[2] The coupling of the Van Allen radiation belts to the Earth's atmosphere through precipitating particles is an area of intense scientific interest, principally due to two separate research activities. One of these concerns the physics of the radiation belts and primarily the evolution of energetic electron fluxes during and after geomagnetic storms [e.g., *Reeves et al.*, 2003] where precipitation losses in to the atmosphere play a major role [*Green et al.*, 2004; *Millan and Thorne*, 2007]. The other focuses on the response of the atmosphere to precipitating particles, with a possible linkage to climate variability [e.g., *Turunen et al.*, 2009; *Seppälä et al.*, 2009, 2013]. Both scientific areas require increased understanding of the nature of the precipitation, particularly with regards to the precipitation drivers, as well as the variation of the flux and energy spectrum for electrons lost from the outer radiation belts.

[3] In both of these areas, it is important to understand the energy range of the electrons lost. For radiation belt physics, relativistic electrons tend to be most important to space systems engineering, but comparatively low-energy electrons (tens of keV) appear to provide the "source population" which is accelerated up to relativistic energies. In addition, the wave-particle interactions which drive acceleration, transport, and loss are dependent upon frequency [e.g., *Tsurutani and Lakhina*, 1997] so that the energy spectra provides evidence of the physical processes occurring. When considering the atmospheric impact of precipitating energetic electrons, the particle energy determines the altitude at which the particle deposits the majority

[1]Department of Physics, University of Otago, Dunedin, New Zealand.
[2]British Antarctic Survey (NERC), Cambridge, UK.
[3]IRAP, CNRS-University of Toulouse, Toulouse, France.

Corresponding author: I. Whittaker, Department of Physics, University of Otago, PO Box 56, Dunedin 9054, New Zealand. (ian.whittaker@otago.ac.nz)

2169-9380/13/10.1002/2013JA019228

of its energy [e.g., *Turunen et al.*, 2009, Figure 3], with ~100 keV electrons causing peak ionization changes at ~80 km altitude and ~1 MeV electron-driven changes peaking at ~62 km altitude. Precipitating charged particles produce odd nitrogen and odd hydrogen in the Earth's atmosphere which can catalytically destroy ozone [*Brasseur and Solomon*, 2005]. Recent experimental studies have demonstrated the direct production of odd nitrogen [*Newnham et al.*, 2011] and odd hydrogen [*Verromen et al.*, 2011; *Andersson et al.* 2012] in the mesosphere by energetic particle precipitation. In particular, *Andersson et al.* [2012] reported experimental evidence of electron precipitation producing odd hydrogen changes, during geomagnetic storms, stretching over the altitude range from ~52 to 82 km, corresponding to electrons from ~100 keV to ~3 MeV.

[4] Clearly, a detailed understanding of the magnitude and energy spectrum of electron precipitation would be of value, along with information on the spatial and temporal variability. Such data sets could be used to compare with space or ground-based data or used to drive a variety of models including chemistry-climate coupled models. Unfortunately, there are very few experimental observations which can fill this role. The majority of scientific and operational spacecraft measuring energetic electron fluxes in the radiation belts report only the total trapped fluxes, as they do not have sufficient angular resolution to resolve the pitch angles of the bounce loss cone (BLC). This will also be true of the Van Allen Probes. Scientific studies on energetic electron losses to date have tended to focus on observations from the Solar Anomalous and Magnetospheric Particle Explorer (SAMPEX) or Polar Orbiting Environmental Satellites (POES) spacecraft, both of which have significant weaknesses. In the case of SAMPEX, the measurements are primarily of the drift loss cone (DLC) rather than the BLC [*Dietrich et al.*, 2010] and are largely limited to an integral electron flux value above ~1 MeV. The Space Environment Monitor instrument carried onboard POES includes a telescope which views some fraction of the BLC [*Rodger et al.*, 2010a] but is again limited by measuring only three integral energy ranges (>30, >100, and >300 keV), while also suffering from significant contamination by low-energy protons [*Rodger et al.*, 2010b].

[5] In this study we rely upon observations from the IDP (Instrument for Detecting Particles) carried onboard the DEMETER (Detection of Electromagnetic Emissions Transmitted from Earthquake Regions) satellite. The IDP is comparatively unusual in that it has very high energy resolution; in normal "survey" mode, the instrument measures electron fluxes with energies from 70 keV to 2.34 MeV, using 128 energy channels [*Sauvaud et al.*, 2006]. With the IDP/DEMETER observations, one can consider how to best describe the energy spectra of electrons in the drift loss cone (DLC) and determine the typical parameters. To aid the determination of electron precipitation values, we analyze 6.5 years of electron energy spectra from the IDP instrument to determine first, the best type of fit and secondly, what the average values are and how they vary with location and geomagnetic activity. From a choice of power law, exponential, and kappa-type fits to the spectra, we show that a power fit generally gives the best results. Standard gradient values for average K_p and McIlwain L shell ranges are given as well as a quantitative description of the behavior during (and after) a geomagnetic storm ($K_p > 5^-$).

2. Finding the Energy Spectrum of Electron Precipitation

2.1. The Three Possible Fit Types

[6] Various approaches have been put forward for fitting the energy spectrum of radiation belt electron fluxes. The most common examples are power laws [e.g., *Rodger et al.*, 2007; *Clilverd et al.*, 2010], *e*-folding [e.g., *Parks et al.*, 1979; *Borovsky and Denton*, 2009], and kappa-type [*Xiao*, 2006]. During this investigation, both power law and *e*-folding distributions will be used in the format shown in equation (1).

$$j_e = \alpha_e e^{\beta_e E} \qquad j_p = \alpha_p E^{\beta_p} \tag{1}$$

Where:

j = flux E = Energy
α = amplitude variable β = gradient variable

The "typical" kappa distribution is a generalized Lorentzian distribution used for fitting hot collisionless space plasmas. This was initially used in 1968 [*Vasyliunas*, 1968] with electron measurements. Many authors have now used the kappa distribution to model high- energy particles (e.g., magnetospheric electrons [*Formisano et al.*, 1973], solar electrons [*Maksimovic et al.*, 1997], and unmagnetized plasmas [*Lazar et al.*, 2012]).

[7] The standard kappa distribution is given below in equation (2). For nonrelativistic plasmas, this can be used without issue; however, the distribution is proportional to $\frac{1}{v^2}^{\kappa+1}$. This means its accuracy will decrease when the particles reach relativistic energies.

$$j = \frac{n_\kappa}{(\pi\kappa v_\kappa^2)^{\frac{3}{2}}} \frac{\Gamma(\kappa+1)}{\Gamma(\kappa-\frac{1}{2})} \left(1 + \frac{v^2}{\kappa v_\kappa^2}\right)^{-(\kappa+1)} \tag{2}$$

Where:

j = flux n_κ = number of particles
κ = spectral index v = particle velocity
v_κ = equivalent thermal speed Γ = Gamma function

Xiao [2006] created the kappa-type distribution which is proportional to momentum rather than speed ($\propto \frac{1}{p}^{\kappa+1}$), meaning that the correct power law is followed at both low and relativistic energies. This distribution was shown to be more accurate than a standard kappa distribution in certain trapped electron spectra in *Xiao et al.* [2008].

$$j = \frac{cE_s(E_s+2)}{E_0} \times \frac{N}{4\pi I} \left[1 + \frac{\sqrt{1+p^2}-1}{\kappa\theta^2}\right]^{-(\kappa+1)} \tag{3}$$

Where:

$$I = \frac{8\beta(\frac{3}{2}, \kappa-2)}{2\kappa-1} \left[3F\left(\kappa+1, \frac{5}{2}; \kappa+\frac{1}{2}; 1-\frac{2}{\kappa\theta^2}\right) + (\kappa-2)F\left(\kappa+1, \frac{3}{2}; \kappa+\frac{1}{2}; 1-\frac{2}{\kappa\theta^2}\right)\right]$$

j = flux $\quad c = 3 \times 10^{10} cms^{-1}$

$E_s = \dfrac{E}{E_0}$ $\quad E$ = K. E. of particles

$E_0 = m_e c^2$ $\quad p$ = momentum of particles

β = beta function $\quad F$ = hypergeometric function

To get to a useful version of the kappa-type distribution for the IDP spectra, we combine equations (4) and (10) in *Xiao et al.* [2008] to create our equation (3). Using the assumption in *Xiao et al.* [2008] that $(\sqrt{1+p_s^2}-1) = E_s$ and using $m_e c^2 \approx 500$ keV, this equation can be rewritten for electron energy spectra fitting purposes. This gives a flux (j) in units of number /cm^2/sr/s/keV as a function of energy (E) in keV.

$$j = 1.2 \times 10^5 E \left(\frac{E}{500} + 2\right) \times \frac{N}{4\pi I}\left[1 + \frac{E}{500\kappa\theta^2}\right]^{-\kappa+1} \quad (4)$$

Using equation (4) gives three fitting parameters. These are κ, the spectral index, N, the plasma number density, and θ, the thermal characteristic parameter.

2.2. Electron Energy Spectrum Instrumentation

[8] The DEMETER satellite was launched in June 2004, flying at an altitude of 670 km (after 2005) in a Sun-synchronous orbit with an inclination of 98°. The satellite performs a north to south pass during the day phase with a local time of 10:30 and performs a south to north pass during the night phase with a local time of 22:30. The final data was received in March 2011 before the deorbiting of the satellite.

[9] The IDP used in this study is an electron spectrometer mounted aboard the DEMETER microsatellite. The IDP has 256 energy channels which can be operated in burst mode (all channels sampled at 1 s) or the more common survey mode (128 channels at 4 s resolution with a constant 17.9 keV bin width), with an energy range from 70 keV to >10 MeV. The burst mode is switched on over specific geographical locations (such as California and Southeast Asia) to fulfill the original mission of the satellite of looking for links between earthquakes and ionospheric changes. The

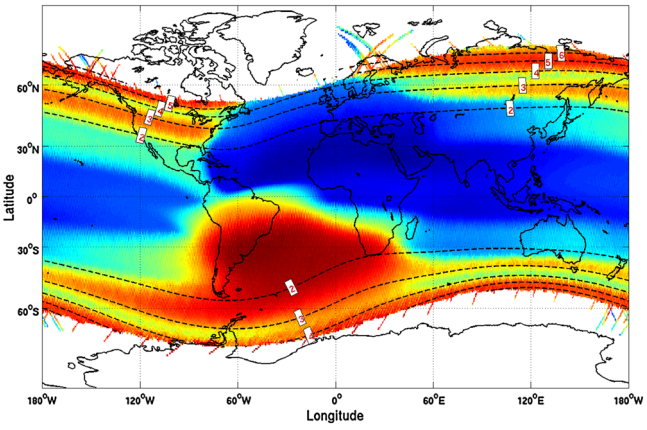

Figure 1. The median integral flux > 93 keV map from all DEMETER IDP data with calculated IGRF L shell values based on satellite altitude shown as contours for the purpose of identifying L shell ranges for analysis. The contours range from L of 2 to 6.

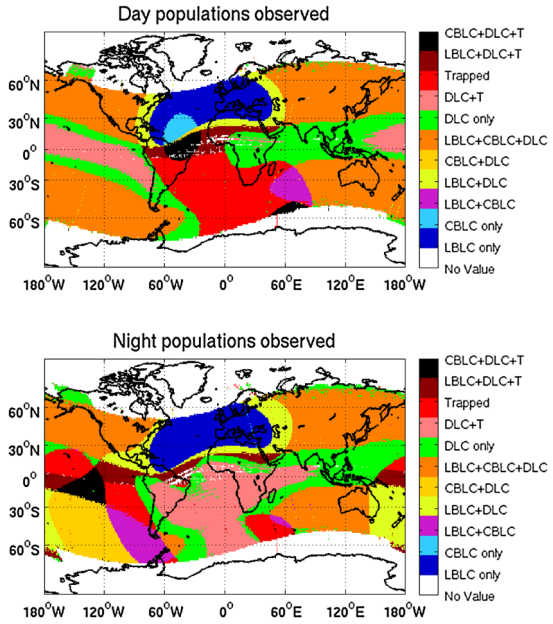

Figure 2. Pitch angle populations sampled by IDP instrument as a function of geographic location for (a) night and (b) day, calculated for 2005. The abbreviation LBLC/CBLC is the local/conjugate bounce loss cone, DLC is the drift loss cone, and T refers to trapped.

detector efficiency is dependent upon the incident angle of the electrons being detected. The detector looks perpendicular to the orbital plane of the satellite, which is almost polar and circular. Due to the geometric configuration of the sensor within the collimator, the exposed sensor area is greatest when viewed from the central axis, and the instrument is therefore most sensitive to incident electrons which are parallel to the central axis. As a smaller fraction of the detector is exposed off axis, sensitivity reduces to zero at angles beyond ±16°.

[10] Electron-induced impulses are detected at a sampling rate of 0.6 MHz in the IDP. The time between the arrival of two incident electrons may be so short that their voltage impulses are indistinguishable to the counting system, giving the appearance of a single high-energy electron arrival. This can lead to a proportion of electron arrivals being misinterpreted, leading to lower flux counts at lower energies and higher flux counts at higher energies giving the spectrum shape a parabolic look rather than an e-folding decay. An example of this is shown in Figure 4 (bottom, left), and the removal of this effect is discussed in section 4, other examples can be seen in *Gamble* [2011]. An opposite effect also exists where high-energy particles (> 1 MeV) can induce a lower-energy flux increase (∼ 300 keV). This occurs because some high-energy electrons are not fully stopped by the detector material registering as a lower-energy impact. This effect is only important when the higher-energy fluxes are large (generally in the South Atlantic Magnetic Anomaly (SAMA)) and are negligible otherwise. The main instrument error at lower energies (i.e., < 1 MeV) is statistical and will be discussed further in section 2.6.

[11] The high-energy resolution IDP/DEMETER observations have already been used to investigate pitch angle

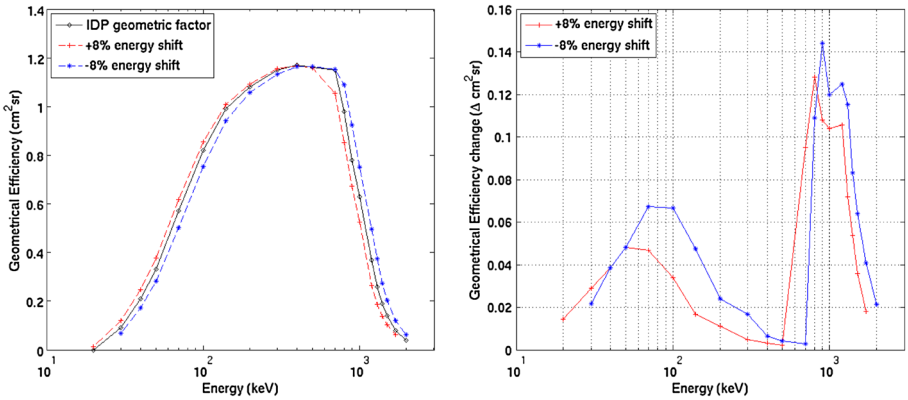

Figure 3. (left) The IDP instrument geometric factor as a function of energy (taken from *Sauvaud et al.* [2006]). The maximum 8% energy resolution error is applied and the appropriate curves are overplotted (The black curve is reprinted from PSS, Vol 54, *Sauvaud et al.* [2006], High-energy electron detection onboard DEMETER: The IDP spectrometer, description and first results on the inner belt, page 506, Copyright (2006), with permission from Elsevier). (right) The difference in flux as a ratio.

scattering of radiation belt electrons and their loss into the atmosphere. For example, previous studies have shown that the powerful U.S. Navy VLF transmitter with call sign North West Cape (NWC) produced >100 keV electron loss cone enhancements around L =1.7–1.9. These enhancements were shown to be consistent with predictions from first-order cyclotron resonance, scattering the electrons into the DLC (drift loss cone) [*Sauvaud et al.*, 2008; *Gamble et al.*, 2008; *Rodger et al.*, 2010a]. The IDP/DEMETER spectral measurements have also been combined with subionospheric VLF observations to determine the time-varying electron precipitation into the atmosphere during and after a geomagnetic storm [*Rodger et al.*, 2010c].

[12] A full description of the instrument can be found in *Sauvaud et al.* [2006].

2.3. Data Sampling

[13] The fitting (power law, *e*-folding, and kappa-type) is performed upon samples of DEMETER IDP data, taking 25 spectra evenly spaced in time from each orbit (where each orbit contains ∼500 spectra). A smaller sample is made up of 14,000 spectra all taken from 11 August 2004 until 9 September 2004, making up 560 orbits of the spacecraft. A larger sample takes the 25 equally spaced spectra, in the same style as the small sample, from every orbit of DEMETER (wherever possible between September 2004 and March 2011) resulting in a sample size of 1,442,800 spectra. The fits are performed on both samples (with the exception of the kappa-type fit which requires a large amount of computer runtime and is hence only performed on the small sample, for more information on this, see Appendix B).

[14] Initially, all data channels from the spectrum were used; however, the burst spectra were immediately obvious as having higher flux than the nearby survey mode spectra. A closer investigation of each energy channel showed an issue with the first energy channel ($E \leq 72$ keV). To remove this particular problem, the first and last energy channels are removed from the fitting procedures, which still leaves 126 channels. This is in a similar style to *Gamble* [2011] who also discarded these two energy channels as they are integrals with unknown energy bounds.

2.4. External Data

[15] The geomagnetic activity index (K_p) values were downloaded from the Space Physics Interactive Data Resource data service [*Space Physics Interactive Data Resource data archive*, 2013] for the length of the DEMETER mission (5.5 years). Geomagnetic field calculations used to determine the pitch angle population sampling are made using the International Geomagnetic Reference Field (IGRF) geomagnetic field model (v.11) developed by *Finlay et al.* [2010], originally ported to MATLAB by Paul O'Brien (paul.obrien@aero.org) in 2003 and updated by Patrick Daum (p.daum@lancs.ac.uk) in 2010.

2.5. Determining Pitch Angle Populations

[16] The median flux value for each DEMETER spectrum (using channels between 2 and 127) is shown in Figure 1. The figure shows that the highest integral fluxes observed occur in the South Atlantic Magnetic Anomaly (SAMA), with other regions such as the inner radiation belt ($2.5 < L < 3$), slot region ($3 < L < 4$), and outer radiation belt ($L > 4$).

[17] When using the flux information provided by the IDP, it is important to know which portion of the pitch angle distribution the instrument is sampling. DEMETER provides the pointing direction of the IDP axis (relative to the local geomagnetic field). Combined with the angular width of the instrument (±16°), and the IGRF [*Finlay et al.*, 2010] specification of the geomagnetic field strength at the local, equatorial, and atmospheric locations, the pointing direction can be used to determine the portion of the pitch angle distribution that is being sampled by the instrument at any particular point.

[18] This is performed by comparing the relevant magnetic field strengths at the equator and at the top of the atmosphere. The atmospheric top is taken to be 110 km altitude from the Earth's surface calculated from DEMETER traced coordinates, this is the height at which the chance

Table 1. The Success Percentage as a Function of r^2 Value for Exponential and Power Fits on Both Small and Large Sample Sets[a]

Exponential Fit			Power Fit		
r^2	Small sample	Large sample	r^2	Small sample	Large sample
0.00	56.4 %	57.1 %	0.00	88.3 %	85.8 %
0.10	54.2 %	54.3 %	0.10	83.8 %	80.7 %
0.20	52.6 %	52.3 %	0.20	80.0 %	76.6 %
0.30	51.0 %	50.6 %	0.30	75.8 %	72.5 %
0.40	49.2 %	49.0 %	0.40	71.7 %	68.3 %
0.50	47.3 %	47.3 %	0.50	67.0 %	64.2 %
0.60	45.3 %	45.2 %	0.60	62.7 %	60.0 %
0.70	42.9 %	42.9 %	0.70	57.1 %	55.2 %
0.80	39.9 %	40.4 %	0.80	47.1 %	48.6 %
0.90	35.8 %	36.5 %	0.90	38.4 %	39.7 %

[a]This comparison shows that the small sample set is acceptable as a sample population.

of a collision from an energetic electron into the neutral atmosphere becomes likely for energies >70 keV.

$$\frac{B_{eq}}{B_{local}} = \frac{\sin^2 \alpha_{eq}}{\sin^2 \alpha_{local}} \quad (5)$$

$$\frac{B_{eq}}{B_{atm}} = \frac{\sin^2 \alpha_{eq}}{\sin^2 \alpha_{atm}} \quad (6)$$

Equations (5) and (6) are used to determine the relevant pitch angle distributions seen once the appropriate magnetic fields have been calculated; this process is described in *Rodger et al.* [2010a, Appendix A] for the POES satellites.

[19] Figure 1 provides context for the various combinations of the trapped (T), drift loss cone (DLC), and bounce loss cone (BLC) populations mapped in Figure 2. The conjugate and local bounce loss cones (CBLC and CDLC) are also shown in Figure 2. We can see from both figures that by not including the data between 90°W and 60°E, we can effectively remove the SAMA, an important consideration that we apply in section 4 to remove contamination of this area from our average global results.

2.6. Instrument Flux Uncertainties

[20] An estimate of the uncertainty in the DEMETER IDP data will be useful when performing fits and doing a superposed epoch analysis. We are not aware that this has appeared in the literature to date.

[21] In *Sauvaud et al.* [2006], it is stated that the energy resolution error is 8%. The flux determination is also described in this paper as the count rate divided by the geometric factor. Thus, by using the maximum energy error, we can obtain maximum values of the flux uncertainty. Figure 3 (left) shows the original energy to geometric factor relation shown in *Sauvaud et al.* [2006]. The dashed red line represents an +8% shift in energy, and the dashed blue line represents a –8% shift. Figure 3 (right) shows the maximum uncertainties as a function of energy, derived from the curve on the left. For energies up to 800 keV, the uncertainty is less than 7% (in the worst case) and has an average value of 3.1%. For energies between 800 keV and 2 MeV, there are significantly higher uncertainties. However, while these reach as much as 15%, they still appear reasonable. It should be noted that up to ∼450 keV the +8% energy shift underestimates the flux and the –8% energy shift overestimates the flux. For energies above 450 keV these shifts swap around.

3. Results

3.1. Initial Values

[22] The power and exponential fits were both applied to the large sample group (and by default, the smaller as well—see section 2.3) using the format shown in equation (1). The

Table 2. The Success Rate of Each Fitting Type Upon the Small and Large Sample Sets[a]

	Confidence Level (CL)			r^2 Value		
Name	90%	95%	99%	0	0.7	0.9
Small Sample (14,000 Spectra)						
Exponential	74,66	7,422	7,342	7,897	6,010	5,006
Power	11,445	11,323	11,141	12,364	7,996	5,382
Kappa-type (free running)	5,249	5,245	5,243	5,253	5,144	5,009
Kappa-type(κ fixed from exp fit)[b]	539	539	539	539	537	531
Kappa-type (κ fixed from power fit)[b]	714	714	714	714	713	701
Large Sample (1,442,800 Spectra)						
Exponential	768,316	760,772	752,469	823,770	620,000	526,199
Power	1,134,288	1,118,083	1,099,413	1,237,399	796,281	573,222

[a]The values are cumulative and show how many spectral fits have an r^2 greater than their column label or above the confidence level, calculated assuming 124 degrees of freedom.

[b]The kappa-type distributions with κ fixed by the exponential or power fit coefficients are only performed on the small sample due to the processing timescale. The process of fixing kappa-type coefficients is described in Appendix A.

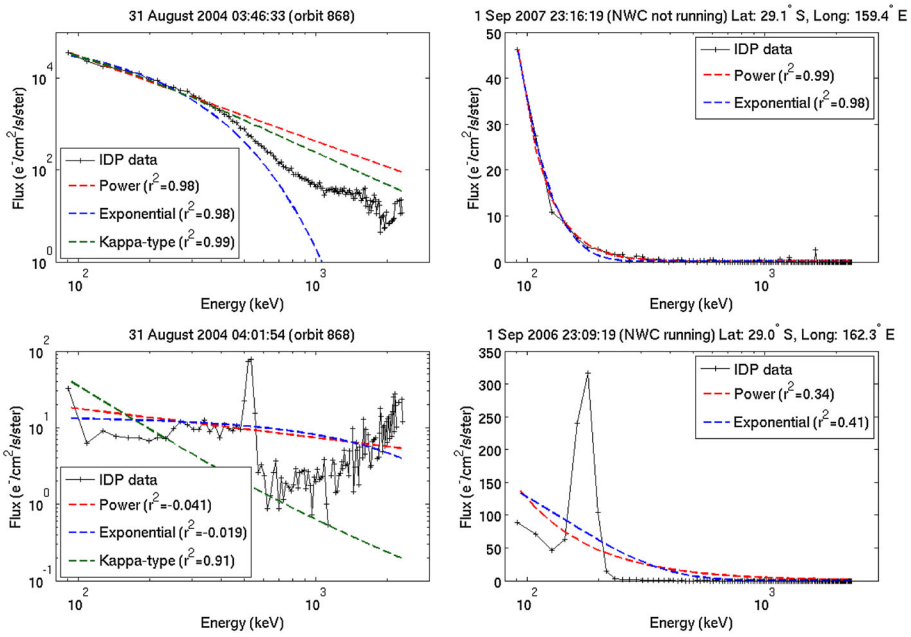

Figure 4. Two examples of where the IDP spectra fits fail. (top, left) A high-flux spectrum in the outer radiation belt and (bottom, left) low flux equatorial spectrum. The three fit types are shown with r^2 values for both spectra. (right) Two spectra from over the Tasman Sea, east of the NWC (North West Cape) radio transmitter. (top, right) NWC is off and (bottom, right) when it is on.

kappa-type distribution was fitted only to the smaller sample of 14,000 spectra due to time and computing constraints and was performed using the Levenberg-Marquardt algorithm as in *Xiao et al.* [2008]. The examples from that paper were recreated first to ensure the equation and fitting method were returning the same results.

[23] The success rates of the exponential and power fits in the small sample set can be seen in Table 1, showing the percentage of spectra with a fitting parameter greater than the appropriate r^2 value for both sample sets. Some of these values can also be seen in Table 2 which shows the absolute numbers of successful fits for each fitting type and includes the kappa-type distribution results. When the success rates of the small and large sample sets are compared in Table 1, the small sample is found to be representative of the whole population. Table 1 also shows the interesting result that at best, 14.2% of the data cannot be fitted at all using the MATLAB fitting procedures, resulting in a negative r^2 value.

[24] Initially, when the kappa-type fitting was performed, the final number of "sensible" (according to Xiao's suggested ranges of the parameter values) fits were very low. Previous work has stated that the κ range (spectral index) is the most important for value comparison, with the lower range at 2 and the upper limit listed as 5 [*Xiao et al.*, 1998] or 6 [*Xiao et al.*, 2008]. To calculate how many fits are usable, we first have to define a range for each parameter based on previous examples by Xiao.

$$2 \leq \kappa \leq 10$$
$$10^{-6} \leq N \leq 10$$
$$10^{-6} \leq \theta \leq 2 \qquad (7)$$

When the range limits are compared to the 6287 original spectral fits with an $r^2 > 0$ in the small sample, only 88 of the values (1.5% of the original number of fits greater than 0) were within all these limits. This is extremely low, so starting conditions were added based on Xiao's examples and within the limits in equation (7) (these are described in Appendix A). This returned 5253 fits with $r^2 > 0$ with the majority of fits having an r^2 value greater than 0.9, the few successful fits within the range of $0 < r^2 < 0.9$ (234 spectra as seen in Table 2) suggest a binary response from the kappa-type fit; it either fails or works with a very high goodness-of-fit.

[25] Figure 4 (left) illustrates the kappa-type fitting problems well. The top left plot (on double $\log_{10}$ axes) is from the outer radiation belt. Here all three fitting types do an excellent job of fitting the data with high r^2 values, and the kappa-type distribution follows a very similar fitting pattern to the power law. The lower left plot shows a low flux equatorial spectrum; unsurprisingly, none of the fit types appear to fit well to the data (mainly due to an increasing flux reported at energies above ~600 keV). In this case the kappa-type parameters are outside of the limits given in equation (7), yet the goodness-of-fit is claimed to be around 0.9. This is due to the kappa-type fit preferring low energies, the first point is very close to the fit, and hence, the actual numerical difference values are low. This is common with the low total flux spectra that have a rising flux in high-energy channels, and this is resolved by adding spectrum-fitting conditions (later described in section 4). With the application of these conditions, the poor kappa-type fits are removed and only the sensible fits are left. The final number of fits with an r^2 value greater than 0 is reduced to 1442 (from 5253) in the small sample (a success rate of 9.7%).

[26] Confidence levels are included along with the goodness-of-fit values in Table 2. As each spectrum included

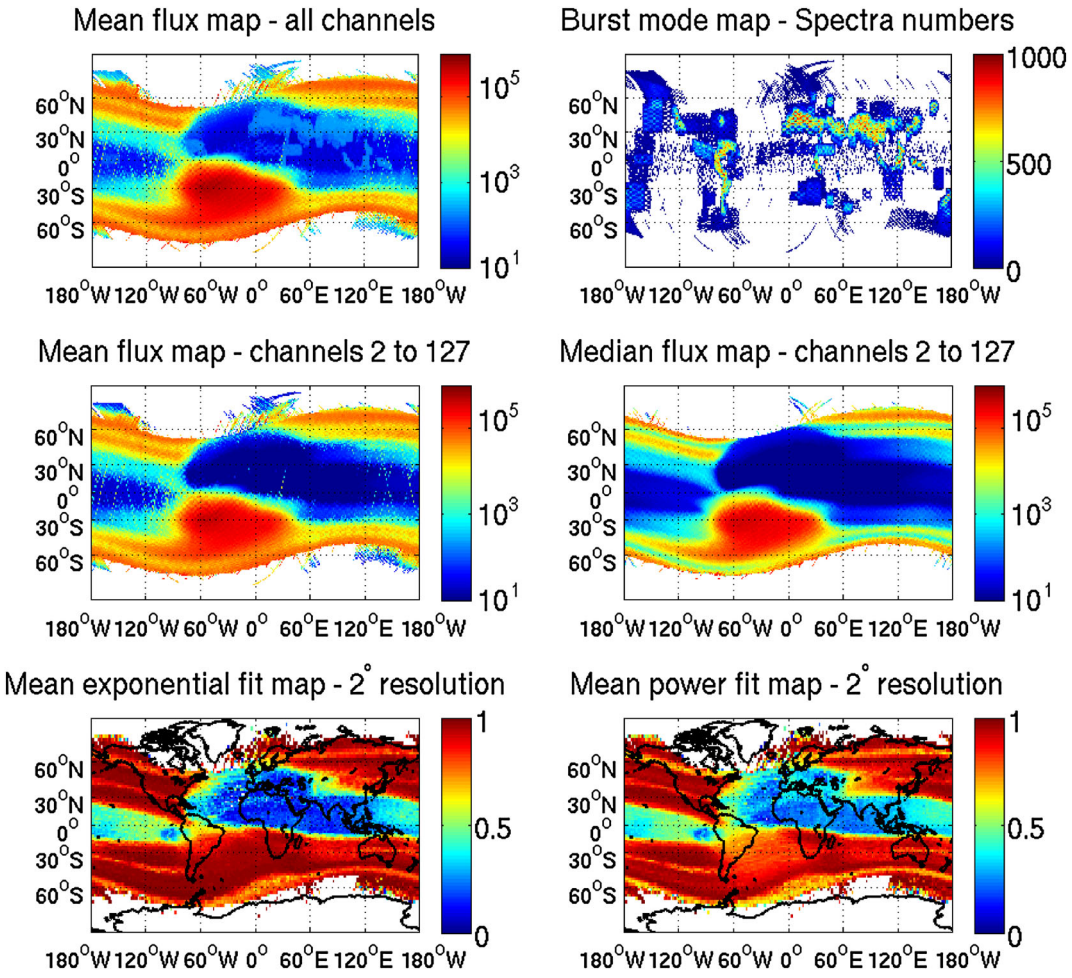

Figure 5. Global maps of the electron flux distribution with a 0.5° bin resolution. (top, left) All channels and (middle, left and right) energy channels 2 to 127. (top, right) Where the burst mode occurs for the large sample data. (middle, left) The mean values and (middle, right) the median which is also shown in Figure 1. The color scale for these plots is $\log_{10}$ flux values. (bottom, left and right) The exponential and power fits shown on a global 2° resolution map. The color scale represents the average r^2 value.

126 data points, the confidence levels were calculated using 124 degrees of freedom (except for the kappa-type which had 123 degrees of freedom, which was a negligible change). The 90%, 95%, and 99% levels are shown, and the power fit consistently performs better than the other fit types. The table also includes the success rates (number of fits greater than the specific r^2 value or confidence interval) of the kappa-type distribution with a fixed κ variable, which is described fully in Appendix A.

3.2. Global Mapping

[27] The integrated flux of each energy channel are binned into a 360 × 720 grid (0.5° latitude and longitude resolution) and displayed in Figure 5. The flux maps contain 38,488,727 entries (all available DEMETER IDP spectra) and have a $\log_{10}$ color scale for integrated flux values (number/cm^2/sr/s).

[28] Figure 5 (top) includes all energy channels from 1 to 128, i.e., including $E \leq 72$ keV and $E > 2.33$ MeV. From these flux maps, the burst mode effect described in section 2.3 can be clearly seen in Figure 5 (top). This appears as the slightly elevated fluxes at approximately 10 counts total around Europe and southern Asia. The mean flux map for the reduced energy range between channels 2 (91 keV) and 127 (2.32 MeV) (middle, left) shows the removal of these burst mode enhancements, but both maps still show the anomalous "hot" orbits. The median map (middle, right and also Figure 1) shows a far smoother global average with the radiation belt limits clearly visible in both hemispheres. Global maps of the exponential and power goodness-of-fit are shown in Figure 5 (bottom). The accuracy of fitting clearly relates to higher-flux regions. The lowest fits in both cases correspond to the areas where total fluxes are less than 100; this approximates to instrument noise, so the lack of fit is unsurprising as the spectra will look similar to Figure 4 (bottom, left).

[29] In both of the fit maps in Figure 5, there are two lower r^2 fit bands in both hemispheres (centering around 60°S, 40°S, 50°N, and 70°N). The more poleward of each of these bands corresponds to the slot region between the

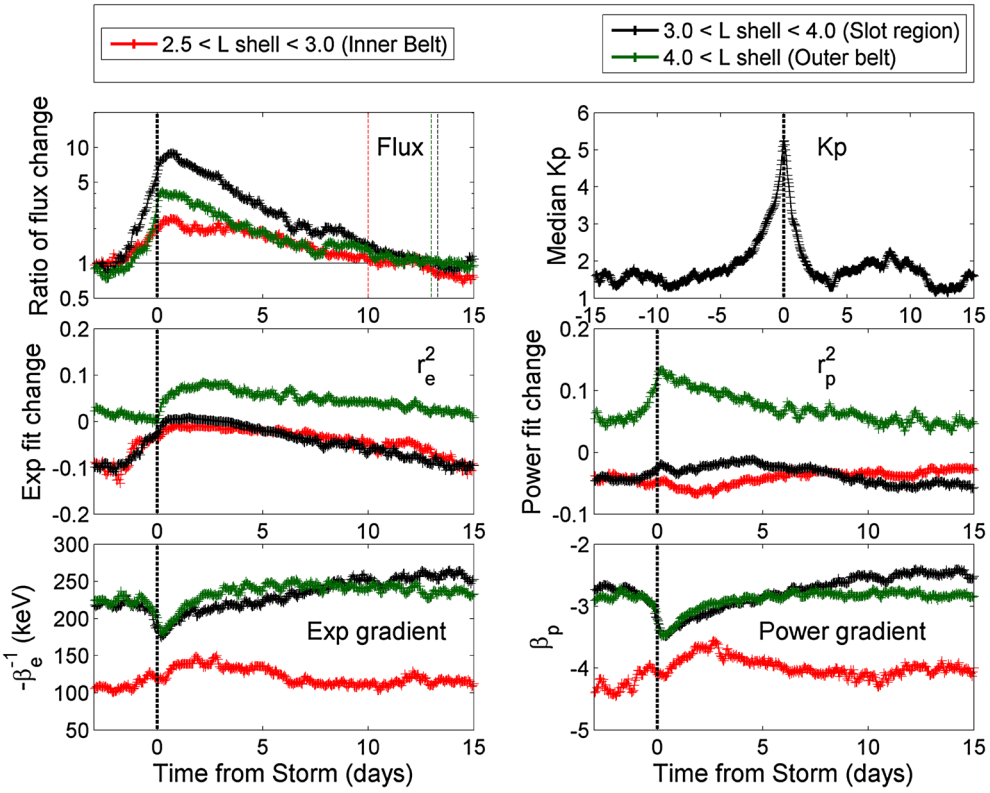

Figure 6. The effects of geomagnetic storm activity on the fitting parameters. (top, left) The median flux intensity change at different times from the storm, the dashed lines represent the time period after which the flux has returned to the average prestorm values. (top, right) The median K_p value around a storm. (middle, left and right) The change in r^2 for the exponential and power fits (the average r^2 values are nonzero) and (bottom, left and right) the actual gradient parameter during a geomagnetic storm ($-\beta_{exp}^{-1}$ and β_{pow}).

radiation belts where the flux drops considerably compared with inside the belts. The more equatorward of the bands, however, corresponds to the effect of the U.S. Navy transmitter NWC, located at the North West Cape on the west coast of Australia (L = 1.45) radiating ~1 MW at 19.8 kHz. This alteration in the fit parameter is caused by the radio transmission pitch angle scattering a specific energy range of electrons within the spectrum, as seen in *Sauvaud et al.* [2008], *Gamble et al.* [2008], and more recently *Li et al.* [2012], causing a reduction of the goodness-of-fit. An example of this is shown in Figure 4 (right), which contains two dayside plots from the approximate same location (Δlatitude = 0.1° and Δlongitude = 2.9°) when the transmitter is on (1 September 2006) and off (1 September 2007 within a period where NWC is shown to be switched off [*Gamble et al.*, 2008]). The effect of the electron flux bulge from "NWC electrons" [*Li et al.*, 2012] is clearly visible in the approximately Gaussian flux increase centered at 180 keV. In this region, the fit quality is lowered causing the band of lower r^2 in Figure 5. Small areas of very high flux also have a fractionally lower r^2 value; this is due to the high-energy tail (described in section 2.2 and shown in Figure 4)

Table 3. The Coefficients to Describe Both the Flux Enhancement Ratio and Also the Power Gradient Around Geomagnetic Storm Time in Equations (8) and (9)

L shell region	a_1	b_1	c_1	a_2	b_2	c_2	a_3	b_3	c_3
				Flux Ratio					
Inner	3.9	12.4	20.3	4.8	73.4	89.5	5.4	160.0	489.3
Slot	26.8	14.1	18.9	25.3	47.2	51.8	13.47	127.3	182.3
Outer	4.0	13.6	18.5	3.5	48.5	46.2	3.0	141.9	245.7
				Gradient					
Inner	–2.5	–60.3	108.4	–0.2	118.0	51.9	–4.1	243.2	307.6
Slot	–0.4	13.0	15.8	–0.8	23.1	101.1	–2.6	179.9	472.0
Outer	–0.5	–11.2	13.1	–0.2	37.0	35.2.7	–2.8	51.1	1786.0

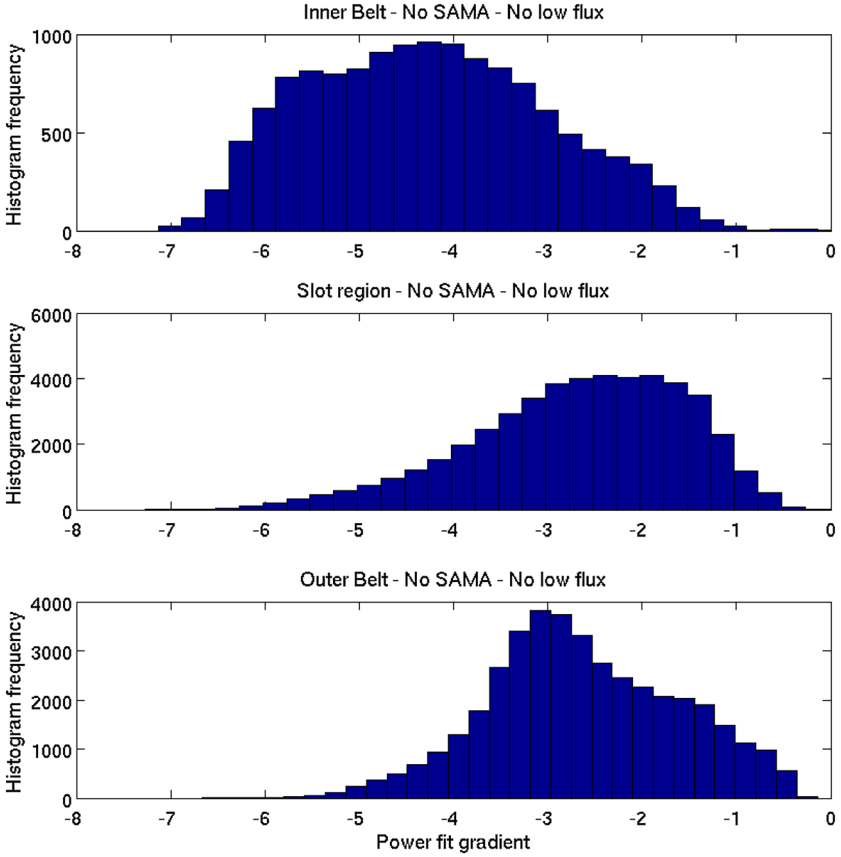

Figure 7. The power fit gradient histograms for each L shell region.

which is removed before the fitting. As the adjusted r^2 value is used, the reduced number of data points lowers the fit value by a small amount.

4. Discussion of Geomagnetic Storm Effects

[30] A geomagnetic storm is divided up into levels dependent upon the K_p value, "K_p of 0 to 4 is below [the] storm, which we label as G0" [*Space Weather Prediction Center*, 2011], meaning that when looking at storm effects, only $K_p \geq 5^-$ are considered. While a comparison of maps is possible at various times from storm onset, the differences between them are difficult to observe. To better illustrate the effects of storm time, we plot Figure 6 where L shell ranges were chosen and median values plotted out against time. The plots in Figure 6 show a superimposed epoch analysis of 721 events where the epoch is defined by a single K_p value $\geq 5^-$ with a time width of 15 days on either side of the K_p event. If multiple geomagnetic storms occur, then the same data can be used again at different times from the storm, although this is not common as Figure 6 (top, right) shows the average K_p event as a single peak.

[31] Rather than choose arbitrary values, the L shell ranges identified from Figure 1 are used (see section 2.5). The four ranges are the following:

[32] 1. $0 \leq$ L shell < 2.5 The regions of low flux largely corresponding to instrument noise.

[33] 2. $5 \leq$ L shell < 3.0 inner radiation belt.

[34] 3. $0 \leq$ L shell < 4.0 slot region between belts.

[35] 4. $0 \leq$ L shell < 6.0 outer radiation belt.

Fitting is not undertaken in the lowest L shell region due to a combination of insufficient flux to perform a good fit and also to avoid the geomagnetic storm ULF resonance effects up to an L shell of 1.9 shown by *Sauvaud et al.* [2013], which will alter any fits performed.

[36] The initial investigation into average gradients at different K_p values came back with values more negative than expected, and an investigation of the fits on the spectra showed that fits were being performed on data which is not considered physical. Three conditions were then imposed to ensure that nonphysical gradients were not included. The first was that a spectrum with a total integrated flux of less than 100 was removed (consistent with the r^2 analysis), and the second that any spectrum with less than 30 nonzero values (approximately 24% of all values) was also not included. The final condition resolves an issue which appears in many spectra and is also shown in Figure 4 (bottom, left). This issue is the increasing flux with higher energies in the tail of the spectrum, as described in section 2.2. The effect can also appear as a set of high-energy spikes rather than a smooth increase, and both can change the fit gradient significantly. To find where this occurs, a linear fit is applied to every spectrum from the middle to the highest energy channel (1.19 MeV to 2.32 MeV). If this linear fit has a positive gradient, then the tail is assumed to curve upward, and only the first half of the energy channels (90 keV to 1.17 MeV) are used in the fit, which results in a more accurate gradient (both visually and also a higher r^2 value).

Table 4. The Median Fit Parameters (Based on Successful Fits Only) for Each L Shell Location at K_p Values up to Storm (5^-)[a]

L shell Region[b]	*e*-Folding (keV)	Power Gradient
	Average	
2.5–3	115.3	–4.04
3–4	231.4	–2.16
4–6	229.1	–2.40
	K_p = 0 to 1	
2.5–3	118.2	–3.93
3–4	250.0	–1.97
4–6	258.6	–2.02
	K_p = 1 to 2	
2.5–3	110.4	–4.22
3–4	220.2	–2.25
4–6	217.1	–2.58
	K_p = 2 to 3	
2.5–3	113.9	–4.12
3–4	207.4	–2.47
4–6	197.5	–2.98
	K_p = 3 to 4	
2.5–3	116.5	–4.07
3–4	202.0	–2.53
4–6	194.1	–3.09
	K_p = 4 to 5	
2.5–3	116.9	–4.09
3–4	203.3	–2.46
4–6	195.7	–2.73

[a]Longitudes including the SAMA are not included.
[b]Where 2.5–3 is the inner belt, 3–4 is the slot region, and 4–6 is the outer belt.

[37] The plots of geomagnetic storm-driven changes with time for the different regions of the radiation belts can be seen in Figure 6, where all data within the SAMA (270° < longitude < 60°) have not been counted toward the median as the observations in this region will contaminate the analysis. Figure 6 (top, left) shows the total flux intensity changes as a ratio of the average value from Figure 1. The clearest result from this plot is that the flux intensity above an L shell of 2.5 increases drastically after the onset of a storm (a result known since *Williams et al.* [1968]). Variations of a factor of ∼2 and 4 are observed in the inner and outer belts, respectively, at the onset of the storm, while the slot region sees a much bigger increase with a factor of about 10 for the normalized values (when the mean values are taken instead, these rise to approximately 8 for both the inner and outer belts and 14 for the slot region). Significant enhancements in flux are observed for approximately 13 days after storm onset when the fluxes return to prestorm values (except for the inner belt which recovers more quickly ∼10 days). These times are shown by the appropriately colored dashed lines which indicate the return to the ratio to 1.

[38] It should be noted that the flux enhancements do not initially start and end at a ratio of 1. An investigation into this shows that the flux response compared to the median map starts above 1 and gradually drops below 1 throughout the lifetime of the instrument, until it reaches March 2010 when there is a step up to above 1 again. This is assumed to be instrument degradation over the 6+ years of data with a voltage change in the last year. The possible options to fix this are to apply a correction factor or to create monthly flux maps to take a ratio from. The correction is difficult to accurately quantize, while producing monthly flux maps would reduce the resolution and hence accuracy of the ratios, so the flux plot in Figure 6 is shown with a normalized value instead. This has no effect on the gradient (β_e or β_p) or on the quality of fit.

[39] The K_p storm values for all the events have a median value of 5, with a lower quartile value of 4.7, and an upper quartile value of 5.7. As the maximum value recorded in this study is 8.7, it suggests that the average response and enhancement values shown here will be most applicable to storms with a lower K_p maximum (between 4.7 and 5.7).

[40] Figure 6 (middle, left and right) shows the r^2 fitting value change from the average values; this represents the difference in time from the high r^2 values seen in Figure 5. These values show that a geomagnetic storm actually increases the goodness-of-fit in the outer radiation belt. This change is not too surprising as the fit coefficient maps in Figure 5 relate very well to the flux maps as previously mentioned. The outer belt increases in flux, and hence, the fit should be better according to this logic. In contrast, the inner belt and slot region goodness-of-fit have a low variation during the storm. Figure 6 (bottom, left and right) shows the gradient of the fit (power gradient (β_p) and *e*-folding energy value ($-\beta_e^{-1}$)). The most important information shown by the gradient parameter is the difference in response between the two belts. Looking at Figure 6 (bottom, left and right), the outer belt spectral gradient decreases (becomes sharper) in β_e and β_p while the inner belt seems to initially follow the same drop in gradient before increasing more strongly in β_e and β_p. The outer belt shows a rapid change at storm onset and then an equally quick transition to a shallower gradient which recovers over a short time frame. The inner belt recovers gradually in a timescale similar to the fluxes (10 days). The slot region very closely resembles the outer belt, and this could be due to the minimum flux condition imposed above which removes the unphysical or noisy spectra.

[41] Equations (8) and (9) describe the behavior of the flux enhancement ratio and the gradient (β_p), respectively. These fits are found by taking the data from 12 h before storm to 312 h afterward. The shape of the curves for both variables means that a triple Gaussian produces the most accurate fit (adjusted $r^2 > 0.95$ in all cases), suggesting there are three processes at work here, other fits with higher degrees of freedom were tried but none came close to describing the shape accurately. The coefficients for each L shell region are shown in Table 3. This model of the gradient behavior and fluxes will allow predictive models to more accurately track precipitation changes during geomagnetic storms to allow for the delay in returning to normal values.

Flux ratio

$$j_r = a_1 e^{-\left(\frac{t-b_1}{c_1}\right)^2} + a_2 e^{-\left(\frac{t-b_2}{c_2}\right)^2} + a_3 e^{-\left(\frac{t-b_3}{c_3}\right)^2} \quad (8)$$

Gradient

$$\beta_p = a_1 e^{-\left(\frac{t-b_1}{c_1}\right)^2} + a_2 e^{-\left(\frac{t-b_2}{c_2}\right)^2} + a_3 e^{-\left(\frac{t-b_3}{c_3}\right)^2} \quad (9)$$

Where: t = time from storm onset

[42] Histograms of the data have been included in Figure 7 for each L shell region, showing the distribution of spectra with corresponding power gradients. The slot and outer belt have a similar shape although with different central points; the inner belt distribution is different, however.

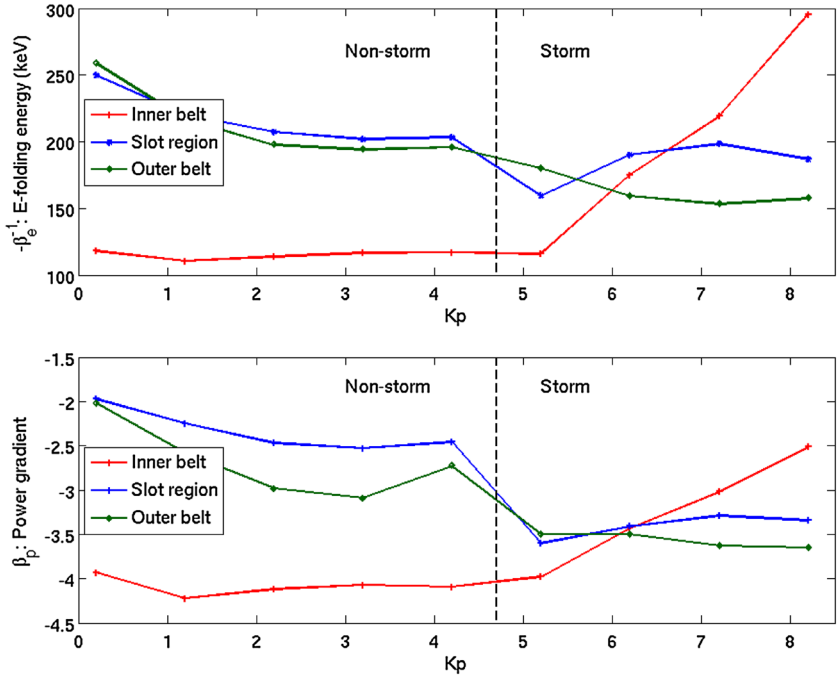

Figure 8. A plot showing the average behavior of gradients of the exponential and power fits with changing K_p. The nonstorm values are taken from Table 4 while the storm values are found by observing the response of Figure 6 when specific K_p ranges are required to count as a storm.

As well as the initial peak around –4, there is also a secondary peak seeming to appear around –5.5. After visual examination of a large number of inner belt spectra, these extreme gradients mainly correspond to spectra which have a positive linear gradient tail which was removed in the analysis. This suggests that the large fluxes which cause the instrument sampling issue described in section 2.2 operates at very low spectral gradients. As this secondary histogram peak is small, we can assume the effect to be negligible.

[43] To get geomagnetic quiet time values the data are separated by K_p value and median values taken (spectra within 96 h after a geomagnetic storm are not included), the storm values are found by taking the peak gradient value within 6 h of storm onset for plots with specific K_p storm conditions. These are shown in Table 4 and Figure 8 along with the overall average values. The spectral slope gradient values show that with increases in K_p, the outer belt and slot region act in a similar way and become sharper ($|\beta_e|$ and $|\beta_p|$ increase) while the inner belt becomes shallower ($|\beta_e|$ and $|\beta_p|$ decrease). Just below typical storm values an interesting effect seems to occur in the slot and outer belt with the gradient moving in the opposite direction to all other values, this is seen in both the exponential and power fit plots.

5. Conclusions

[44] In this study we have investigated how to find the best fit to DEMETER IDP data. The evidence from Figure 5 and Table 2 suggest that of the three fit types investigated (power law, exponential, and kappa-type), the power law fit is consistently the best to use. The higher success rates across all r^2 values and confidence levels are the main factors in this conclusion. In terms of location then there is a direct correlation between high flux and high quality of fit, the best locations to give a reasonable fit are anywhere poleward of the –30° to 30° geographic latitude region, i.e., from the inner radiation belt outward and not in the SAMA.

[45] The relevance of the kappa-type fits is a more difficult issue, mainly due to the fact that several different combinations of variables will fit the DEMETER IDP data. This means that unguided, the fit routine will more likely fall into local fitting minima. As described in Appendix A, giving a startpoint to the fitting routine results in a high success rate with physical variables returned. Looking at the examples of typical orbits in Figure 4, it appears that the kappa-type fit produces a similar fit to the power law but is biased toward the low-energy electrons. If the energy range of the IDP instrument went down to lower electron energies, then the kappa-type fit would be more appropriate than it currently is. However, when using IDP observations, it is recommended that users fit with the power law.

[46] Values for the gradient (β_e and β_p) of fits are determined for various K_p and L shell ranges, which should assist with the input data for various atmospheric models investigating the link between geomagnetic activity and climate variability [*Seppälä et al.*, 2009]. Included as part of this fit description is the effect of increased geomagnetic activity and the response of the gradient and fluxes until recovery, thus allowing a large percentage of all possible points to be accurately modeled. These are shown in Table 4, Figures 6 and 8, and equations (8) and (9). An important conclusion to take from this is that the recovery time after a storm is of the order of 13 days for the slot and outer belt and approximately 10 days for the inner belt; once the K_p has returned to low values, the flux enhancements are still observable. Hence, relating flux to the K_p value directly is not necessarily valid following a period of geomagnetic storm activity. The

difference in times of the flux enhancement recovery can be put down to the lifetimes of particles being affected by the plasmapause; publications looking at extreme events [e.g., *Shprits et al.*, 2006; *Thorne et al.*, 2013] have shown that the compression or expansion of the plasmapause changes the conditions at higher L shells as well as tracking the inner boundary of the outer radiation belt.

[47] The uncertainties in the flux values shown in section 2.6 and Figure 3 are well below 10% until an energy value around 800 keV is reached. At these energies, the fluxes are very low and thus will make little impact on the fitting. The uncertainty might also be an additional factor in the creation of the high-energy tails shown in Figure 4 (bottom, left).

[48] We find in this study that the median fluxes in the DLC (from Figure 2, with the removal of the SAMA longitudes, this is the main area sampled and hence represents nontrapped particles) typically increase by a factor of 2 to 4 after storms (∼10 for the slot region), although this is highly variable and likely linked to storm intensity. When restrictions are placed on the minimum value of K_p for a storm, this flux enhancement rises significantly. These values are consistent with previous observations of changing DLC fluxes shown in *Clilverd et al.* [2010, Figure 8]. POES and DEMETER data showed DLC flux variations of 1–2 orders of magnitude while local BLC flux variations reported in that paper show larger variations (i.e., 2 orders of magnitude in POES data and 4 orders of magnitude in the ground-based subionospheric Antarctic-Arctic Radiation-belt Dynamic Deposition VLF Atmospheric Research Konsortia observations). The smaller variations in the DLC rather than the BLC may be due to pitch angle scattering occurring localized in MLT, which drive large spatially localized BLC changes. These are only part of the contribution to DLC fluxes, as they represent longitudinally integrated scattering processes.

[49] From Table 2 and Figure 5, the reader can decide which fit to use depending on their preferences; however, it is clear that using a power law is going to give the best results, due to its high number of fitting successes at high confidence levels.

Appendix A: Fixing Kappa-Type Fitting Parameters

[50] From the initial kappa-type distribution fits in Table 2, we can see that the success rate is low within the given limits. Constraining the kappa fit to the limits in equation (7), more often than not, results in a fitting error in MATLAB. This can only be put down to the fact that small data variations in the spectrum can cause large differences within the beta and geometric functions. It should also be noted that the starting conditions have a very large effect on how well the MATLAB fitting algorithms perform as described in section 3.1. The starting point settled upon for these fits are an average of the examples: $\kappa = 4$, $N = 0.1$, and $\theta = 0.02$. As seen in Table 2, the success rate with this starting point is not diminished by much (5253–38%) and produces more accurate coefficients. The frequency of success is also linked to the burst mode of the instrument; in the low flux areas where the burst mode is active (such as Mexico and Japan), the kappa-type fit is better than nonburst mode areas.

[51] The fixing of κ produced a large number of fits with $\kappa \leq 2$ which results in all fluxes being zero. This occurs because of the β function in equation 4, with a κ value of 2, or less the second term of the function is 0 or negative resulting in an infinity term. When put into the full kappa-type equation, this results in $\frac{N}{\text{inf}}$ giving a multiplication factor of 0. MATLAB calculates the goodness-of-fit (r^2) as being better than 0.9 in this case which is an obvious error similar to Figure 4. The success rates of the fixed variable kappa-type fits are shown in Table 2 for when $\kappa > 2$ and with this constraint added are very low, and hence, analysis is not continued.

Appendix B: Processing Times

[52] This appendix covers the processing time required by different methods on a modern desktop machine. Evidently this will be strongly affected by the power of the machine being used, but the relative time differences could be of use to other researchers when using DEMETER/IDP data.

[53] 1. Small sample (14,000 spectra)

***Exponential and power fit*:** 150 min
***Kappa-type fit*:** 38 min
***Kappa-type (1 variable bound) fit*:** 54.5 h
***Kappa-type (2 variables bound) fit*:** 100 min
***Kappa-type (all variables bound) fit*:** 4 min

[54] 2. Large sample (1,442,800 spectra)

***Exponential and power fit*:** 18 days (approximate)
***Kappa-type (all variables bound) fit*:** 13 h

[55] 3. All data (31,353,274 spectra)

***Flux mean map*:** 6 h
***Flux median map*:** 26 days (approximate)

The time process for fixing extra variables in the kappa-type fit has also been included as this was performed but not reported due to the exceptionally low-fitting success. It should be noted that the speed of the free-running kappa-type fit is fast compared to the other fit types mainly due to the fact that MATLAB rapidly fails to provide a fit for the three variables and skips to the next spectrum quite frequently.

[56] **Acknowledgments.** The research leading to these results has received funding from the European Community's Seventh Framework Programme (FP7/2007-2013) under grant agreement 263218.

[57] Masaki Fujimoto thanks the reviewers for their assistance in evaluating this paper.

References

Andersson, M., P. T. Verronen, S. Wang, C. J. Rodger, M. A. Clilverd, and B. R. Carson (2012), Precipitating radiation belt electrons and enhancements of mesospheric hydroxyl during 2004–2009, *J. Geophys. Res.*, *117*, D09304, doi:10.1029/2011JD017246.

Borovsky, J. E., and M. H. Denton (2009), Electron loss rates from the outer radiation belt caused by the filling of the outer plasmasphere: The calm before the storm, *J. Geophys. Res.*, *114*, A11203, doi:10.1029/2009JA014063.

Brasseur, G., and S. Solomon (2005), *Aeronomy of the Middle Atmosphere,* 3rd ed., D. Reidel Publishing Company, Dordrecht.

Clilverd, M. A., C. J. Rodger, R. J. Gamble, T. Ulich, T. Raita, A. Seppälä, J. C. Green, N. R. Thomson, J.-A. Sauvaud, and M. Parrot

(2010), Ground-based estimates of outer radiation belt energetic electron precipitation fluxes into the atmosphere, *J. Geophys. Res.*, *115*, A12304, doi:10.1029/2010JA015638.

Dietrich, S., C. J. Rodger, M. A. Clilverd, J. Bortnik, and T. Raita (2010), Relativistic microburst storm characteristics: Combined satellite and ground-based observations, *J. Geophys. Res.*, *115*, A12240, doi:10.1029/2010JA015777.

Finlay, C. C., et al. (2010), International geomagnetic reference field: The eleventh generation, *Geophys. J. Int.*, *183*, 1216–1230, doi:10.1111/j.1365-246x.2010.04804.x.

Formisano, V., G. Moreno, and F. Palmiotto (1973), Solar wind interaction with the Earth's magnetic field: 1. Magnetosheath., *J. Geophys. Res.*, *78*(19), 3714–3730, doi:10.1029/JA078i019p03714.

Gamble, R. J. (2011), The 17–19 January 2005 atmospheric electron precipitation event, PhD thesis, Department of Physics, University of Otago.

Gamble, R. J., C. J. Rodger, M. A. Clilverd, J.-A Sauvaud, N. R. Thomson, S. L. Stewart, R. J. McCormick, M. Parrot, and J.-J. Berthelier (2008), Radiation belt electron precipitation by man-made VLF transmissions, *J. Geophys. Res.*, *113*, A10211, doi:10.1029/2008JA013369.

Green, J. C., T. G. Onsager, T. P. O'Brien, and D. N. Baker (2004), Testing loss mechanisms capable of rapidly depleting relativistic electron flux in the Earth's outer radiation belt, *J. Geophys. Res.*, *109*, A12211, doi:10.1029/2004JA010579.

Lazar, M., P. Yoon, and R. Schlickeiser (2012), Spontaneous electromagnetic fluctuations in unmagnetized plasmas. III. Generalized kappa distributions, *Phys. Plasmas*, *19*(12), 122108, doi:10.1063/1.4769308.

Li, X., et al. (2012), Study of the North West Cape electron belts observed by DEMETER satellite, *J. Geophys. Res.*, *117*, A04201, doi:10.1029/2011JA017121.

Maksimovic, M., V. Pierrard, and P. Riley (1997), Ulysses electron distributions fitted with Kappa functions, *Geophys. Res. Lett.*, *24*(9), 1151–1154.

Millan, R. M., and R. M. Thorne (2007), Review of radiation belt relativistic electron loss, *J. Atmos. Sol. Terr. Phys*, *69*, 362–377, doi:10.1016/j.jastp.2006.06.019.

Newnham, D. A., P. J. Espy, M. A. Clilverd, C. J. Rodger, A. Seppälä, D. J. Maxfield, P. Hartogh, K. Holmén, and R. B. Horne (2011), Direct observations of nitric oxide produced by energetic electron precipitation in the Antarctic middle atmosphere, *Geophys. Res. Lett.*, *38*, L20104, doi:10.1029/2011GL049199.

Parks, G. K., C. Gurgiolo, and R. West (1979), Relativistic electron precipitation, *Geophys. Res. Lett.*, *6*(5), 393–396, doi:10.1029/GL006i005p00393.

Reeves, G. D., K. L. McAdams, R. H. W. Friedel, and T. P. O'Brien (2003), Acceleration and loss of relativistic electrons during geomagnetic storms, *Geophys. Res. Lett.*, *30*(10), 1529, doi:10.1029/2002GL016513.

Rodger, C. J., M. A. Clilverd, N. R. Thomson, R. J. Gamble, A. Seppälä, E. Turunen, N. P. Meredith, M. Parrot, J.-A. Sauvaud, and J.-J. Berthelier (2007), Radiation belt electron precipitation into the atmosphere: Recovery from a geomagnetic storm, *J. Geophys. Res.*, *112*, A11307, doi:10.1029/2007JA012383.

Rodger, C. J., B. Carson, S. Cummer, R. J. Gamble, M. Clilverd, J. Green, J.-A. Sauvaud, M. Parrot, and J.-J. Berthelier (2010a), Contrasting the efficiency of radiation belt losses caused by ducted and nonducted whistler-mode waves from ground-based transmitters, *J. Geophys. Res.*, *115*, A12208, doi:10.1029/2010JA015880.

Rodger, C. J., M. A. Clilverd, J. Green, and M. Lam (2010b), Use of poes SEM2 observations to examine radiation belt dynamics and energetic electron precipitation in to the atmosphere, *J. Geophys. Res.*, *115*, A04202, doi:10.1029/2008JA014023.

Rodger, C. J., M. A. Clilverd, A. Seppälä, N. R. Thomson, R. J. Gamble, M. Parrot, J.-A. Sauvaud, and T. Ulich (2010c), Radiation belt electron precipitation due to geomagnetic storms: Significance to middle atmosphere ozone chemistry, *J. Geophys. Res.*, *115*, A11320, doi:10.1029/2010JA015599.

Sauvaud, J.-A, T. Moreau, R. Maggiolo, J. Treilhou, C. Jacquey, A. Cros, J. Coutelier, J. Rouzard, E. Penou, and M. Gangloff (2006), High-energy electron detection onboard DEMETER: The IDP spectromoeter, description and first results on the inner belt, *Planet. Space Sci.*, *54*(5), 502–511, doi:10.1016/j.pss.2005.10.019.

Sauvaud, J.-A., R. Maggiolo, C. Jacquey, M. Parrot, J.-J. Berthelier, R. J. Gamble, and C. J. Rodger (2008), Radiation belt electron precipitation due to VLF transmitters: Satellite observations, *Geophys. Res. Lett.*, *35*, L09101, doi:10.1029/2008GL033194.

Sauvaud, J.-A., M. Walt, D. Delcourt, C. Benoist, E. Penou, Y. Chen, and C. T. Russell (2013), Inner radiation belt particle acceleration and energy structuring by drift resonance with ULF waves during geomagnetic storms, *J. Geophys. Res. Space Physics*, *118*, 1723–1736, doi:10.1002/jgra.50125.

Seppälä, A., C. E. Randall, M. A. Clilverd, E. Rozanov, and C. J. Rodger (2009), Geomagnetic activity and polar surface level air temperature variability, *J. Geophys. Res.*, *114*, A10312, doi:10.1029/2008JA014029.

Seppälä, A., H. Lu, M. A. Clilverd, and C. J. Rodger (2013), Geomagnetic activity signatures in wintertime stratosphere wind, temperature and wave response, *J. Geophys. Res. Atmospheres*, *118*, 2169–2183, doi:10.1002/jgrd50236.

Shprits, Y. Y., R. M. Thorne, R. B. Thorne, S. A. Glauert, M. Cartwright, C. T. Russell, D. N. Baker, and S. G. Kanekal (2006), Acceleration mechanism response for the formation of the new radiation belt during the 2003 Halloween solar storm, *Geophys. Res. Lett.*, *33*, L05104, doi:10.1029/2005GL024256.

Space Physics Interactive Data Resource data archive, N. G. D. Center/NOAA. (2013), *Geomagnetic Indicies, Retrieved February 1, 2013*. [Available at http://spidr.ngdc.noaa.gov/spidr/basket.do.]

Space Weather Prediction Center, NOAA. (2011), *The K-index, Retrieved February 1, 2013*. [Available at http://www.swpc.noaa.gov/info/Kindex.html.]

Thorne, R. M., et al. (2013), Evolution and slow decay of an unusual narrow ring of relativistic electrons near L 3.2 following the September 2012 magnetic storm, *Geophys. Res. Lett.*, *40*, 3507–3511, doi:10.1002/grl.50627.

Tsurutani, B. T., and G. S. Lakhina (1997), Some basic concepts of wave-particle interactions in collisionless plasmas, *Rev. Geophys.*, *35*(4), 491–501, doi:10.1029/97RG02200.

Turunen, E., P. T. Verronen, A. Seppälä, C. J. Rodger, M. A. Clilverd, J. Tamminen, C. F. Enell, and T. Ulich (2009), Impact of different energies of precipitating particles on NOx generation in the middle and upper atmosphere during geomagnetic storms, *J. Atmos. Sol. Terr. Phys.*, *71*, 1176–1189, doi:10.1029/2002GL016513.

Vasyliunas, V. (1968), A survey of low-energy electrons in the evening sector of the magnetosphere with OGO 1 and OGO 3, *J. Geophys. Res.*, *73*, 2839–2884.

Verronen, P. T., C. J. Rodger, M. A. Clilverd, and S. Wang (2011), First evidence of mesospheric hydroxyl response to electron precipitation from the radiation belts, *J. Geophys. Res.*, *116*, D07307, doi:10.1029/2010JD014965.

Williams, D., J. Arens, and L. Lanzerotti (1968), Observations of trapped electrons at low and high altitudes, *J. Geophys. Res.*, *73*(17), 5673–5696, doi:10.1029/JA073i05673.

Xiao, F. (2006), Modelling energetic particles by a relativistic kappa-loss-cone distribution function in plasmas, *Plasma Phys. Controlled Fusion*, *48*(2), 203–213, doi:10.1088/0741-3335/48/2/003.

Xiao, F., R. Thorne, and D. Summers (1998), Instability of electromagnetic R-mode waves in a relativistic plasma, *Phys. Plasmas*, *5*(13), 2489–2497, doi:10.1063/1.872932.

Xiao, F., C. Shen, Y. Wang, H. Zheng, and W. Shui (2008), Energetic electron distributions fitted with a relativistic kappa-type function at geosynchronous orbit, *J. Geophys. Res.*, *113*, A05203, doi:10.1029/2007JA012903.